Expected Recurrence of Extreme Winds in Northwestern Sahara and Associated Uncertainties

Elena García Bustamante [1,*] **, J. Fidel González Rouco** [2] **, Jorge Navarro** [1] **, Etor E. Lucio Eceiza** [3,4] **and Cristina Rojas Labanda** [2]

[1] Departmento de Energía, Centro de Investigaciones Energeticas, Medioambientales y Tecnologicas (CIEMAT), 28040 Madrid, Spain; jorge.navarro@ciemat.es

[2] Department Física de la Tierra, Astronomía y Astrofísica, Universidad Complutense de Madrid-Instituto de Geociencias (CSIC-UCM), 28040 Madrid, Spain; fidelgr@ucm.es (J.F.G.R.); crisroja@ucm.es (C.R.L.)

[3] Institute of Meteorology, Freie Universtität Berlin, 12165 Berlin, Germany; lucio-eceiza@dkrz.de

[4] Deutsches Klimrechenzentrum Gmbh (DKRZ), 20146 Hamburg, Germany

[*] Correspondence: elena.garcia2@ciemat.es; Tel.: +34-91-3466-3609

1. Data

1.1. Observed wind data

Table S1 summarizes the wind data available for this study. This includes the geographical coordinates, the period spanned by the records, the height of the sensors and their elevation, the temporal resolution of the original data and whether maximum wind gust (3-sec averages) and/or 10-min averages of wind speed values are available at the corresponding site.

As it is well known and extensively referenced in the literature, dealing with meteorological observations involves many problems and inconsistencies of different types that have the potential of directly impacting the quality of the dataset. The QC procedure developed in the present study is structured in three main steps that involve the detection and suppression of *rough errors*: (1) manipulation errors (such as artificial data repetitions); (2) unrealistic values and ranges in wind speed and direction; (3) variations that are abnormally high or low (e.g., long periods of constant values or calms). Furthermore, an inspection and suppression (correction in the case of the wind direction) of *systematic errors* was also applied. The wind speed and wind direction data are assessed independently, although most of the steps are common for the two variables. The techniques applied are described in [1] and in [2,3]

1.2. High-resolution simulation over the northwestern Sahara

Data from the ERA-Interim reanalysis [4] have been used as initial and boundary conditions to drive the mesoscale model [5]. WRF was spatially configured with three domains in order to progressively reach the desired horizontal resolution (see Figure S1). The model is initialized as a "cold start" at 0 hours of each day and is run for 48 hours. The first 24 hours are discarded as model spin-up.

In this study, the selected physical configuration of the WRF model was based on [6,7]. The long wave radiation is represented with a Rapid Radiative Transfer Model [8], while the shortwave radiation scheme is based on [9]. A modified version of the [10,11] scheme is used for the cumulus parameterization. The YSU PBL parameterization [12] is used in the three domains. With respect to the microphysics, the WRF Single-Moment six-class scheme, similar to [13], is included. The Noah land-surface model is used to provide the heat and moisture fluxes at land points [14]. Finally, a surface layer model based on the similarity theory was chosen [7]. For more specific details on the parameterizations, the reader is referred to [15].

The mean wind speed at 10 m above the ground level (a.g.l) during the period 2002–2014 from the ERA-Interim reanalysis fields and from the WRF simulation are represented

Table S1: Information of sites with meteorological records (see also Figure 1 of the main text). Columns indicate the label assigned to the site, the geographical coordinates, the initial and final date with data availability, the sensor height a.g.l (-9999 implies unknown), the elevation a.s.l. and the temporal resolution (1-, 10- or 30-min; 3 hourly; or 1 day) for each site. All sites provide quasi-instantaneous (defined as an average during the last 1/10-min previous to the measuring time) wind speed in ms^{-1} except for METxx, which provides the maximum daily wind gust and some IMPxx that provide both variables.

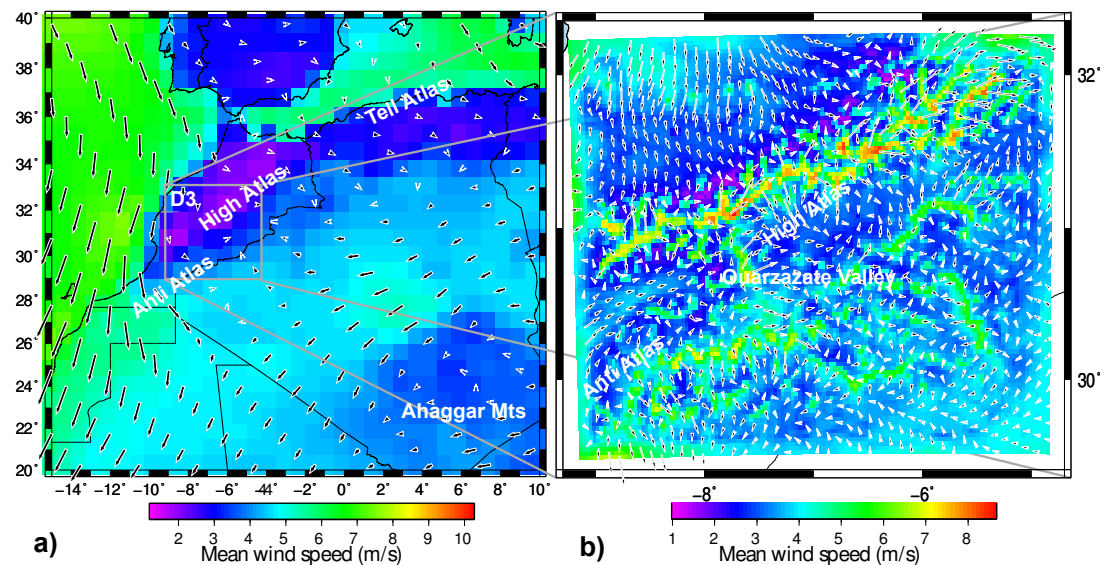| Name	Lat	Lon	Ini. Date	Fin. Date	Height	Elev.	Temp. resol	Variables	
	(^{0})	(^{0})	(yyyymmdd)	(yyyymmdd)	(m)	(m)		10m	gust
NCA02	32.28	-9.23	19990930	20141018	10	50	3h	yes	no
NCA03	32.53	-6.28	19990930	20141018	10	550	3h	yes	no
NCA04	32.37	-6.40	19990930	20141018	10	450	3h	yes	no
NCA05	32.68	-4.73	19990930	20141018	10	1470	3h	yes	no
NCA06	31.94	-4.40	19990930	20110213	10	970	3h	yes	no
NCA07	31.52	-9.78	19990930	20141018	10	0	3h	yes	no
NCA16	30.32	-9.41	19991001	20141018	10	140	30m	yes	no
NCA17	31.94	-4.40	20110214	20141018	10	970	30m	yes	no
NCA18	31.60	-8.03	19991001	20141018	10	440	30m	yes	no
NCA19	30.93	-6.90	19991001	20141018	10	1136	30m	yes	no
MET01	30.93	-6.90	20020101	20141231	10	1136	1d	no	yes
MET02	31.93	-6.40	20020101	20141231	10	1037	1d	no	yes
IMP01	30.36	-5.84	20010918	20080317	3	-9999	10m	yes	no
IMP02	30.36	-5.63	20001116	20080930	3	-9999	15m	yes	yes
IMP03	29.97	-6.35	20011108	20081002	3	-9999	10m	yes	no
IMP04	29.94	-5.63	20020101	20080331	3	-9999	15m	yes	yes
IMP05	30.96	-6.34	20011023	20080930	3	-9999	15m	yes	no
IMP06	31.50	-6.25	20010405	20081008	3	-9999	15m	yes	no
IMP07	31.50	-6.45	20011008	20080325	3	-9999	15m	yes	yes
IMP08	31.39	-6.32	20011021	20081019	3	-9999	15m	yes	no
IMP09	31.54	-6.30	20010404	20080324	3	-9999	15m	yes	no
IMP10	31.17	-6.58	20010410	20081024	3	-9999	15m	yes	yes
IMP11	31.57	-6.30	20011018	20081009	3	-9999	15m	yes	no

Figure S**1.** Spatial configuration of the domains used for the regional simulations: three domains using one-way nesting at 27 km (D1), 9 km (D2) and 3 km (D3) of horizontal resolution. The orography is represented at the corresponding resolution for each domain (see shading scale).

in Figs. S2a and S2b. The reanalysis wind field is shown for the broader northwestern African region with a horizontal resolution of 81 km. Higher wind speeds are simulated at the northwestern coasts and over the Atlas Mountains. Mean winds are weaker over the Sahara and to the SE of the Atlas and increase again over the Ahaggar Mountains in southern Algiers. The mean wind direction is from the NW, favored by the subtropical Azores High, borders the Atlas Range to the south and interior. The southern regions of the Atlas are exposed, on average, to NE winds, diverted from the Mediterranean and around the Tell Atlas. The largest wind speeds over the Atlas reach in the reanalysis *ca.* 2 ms^{-1} on average for the whole period.
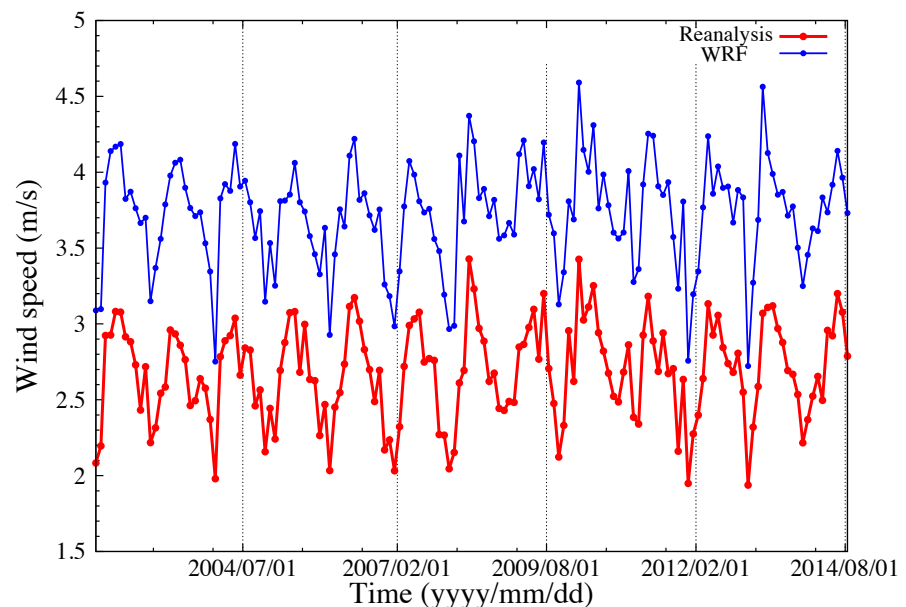
The mean wind speeds simulated by WRF over the D3 domain (Figure S2b) demonstrates considerably higher values with more realistic spatial variability and more complex detail related to a finer topography compared to the reanalysis. Over the north of the High Atlas, the dominant wind direction is from the N and NW in consistency with reanalysis. To the south of the Atlas, a more complex arrangement of directions is simulated, with mean winds from the E and SE near the coast channeling along the Ouarzazate valley, where counter clockwise circulations are produced between the High Atlas and the Anti Atlas. Over the South and East area within the High Atlas and the Anti Atlas, the mean wind flow describes a complex structure broadly following the distribution of mountains and valleys. Hereafter, the simulated wind at 10 m from the D3 domain is used since it is compared to the surface wind provided by the observations, which are mostly sampled at this height.

The temporal variability of the monthly mean wind from both the reanalysis and the WRF simulation (averaged over D3 domain) is as well represented in Figure S3 for comparison. The annual cycle is evidenced with the largest (lowest) mean wind speeds occurring in summer (winter). Due to the relatively large spatial domain used to calculate the temporal averages, the wind variations compare reasonably well in both cases. Further differences between the WRF simulation and the reanalysis are more noticeable when local scales and higher temporal resolutions (e.g., daily) are considered. The largest wind speeds over the whole region occurred in the summers of 2008, 2010 and 2013. The winters of

Figure S**2.** Mean simulated wind speed and wind direction at 10 m a.g.l. from a) ERA-Interim reanalysis over NW Africa and b) from the inner-most D3 domain (3 km) of the WRF simulation (right). Averages were obtained over the whole period of simulation, 2002–2014. Shading indicates the mean wind speed, and arrows represent the average wind intensity and direction.

2004, 2005, 2012 and 2013 showed the lowest mean wind speeds. It should be noted that these are regional averages, and local wind extremes may not necessarily coincide with the windiest seasons on average. It is also noticeable that the regional wind simulated by WRF is, on average, about 1 ms^{-1} larger than that of the reanalysis as a result of the increase of resolution and the better representation of the mountain regions.

Figure S**3.** Monthly mean wind speed time series at 10 m a.g.l. for the reanalysis (red) and for the WRF simulation (blue) averaged over the D3 domain.

1.3. Comparison of observed and simulated wind

In order to ensure robustness to the estimation of the occurrence of extreme winds based on simulated wind return values, it is advisable to compare the simulated and

observed wind fields as a means of evaluating the confidence on the model realism to reproduce the observed wind variability.
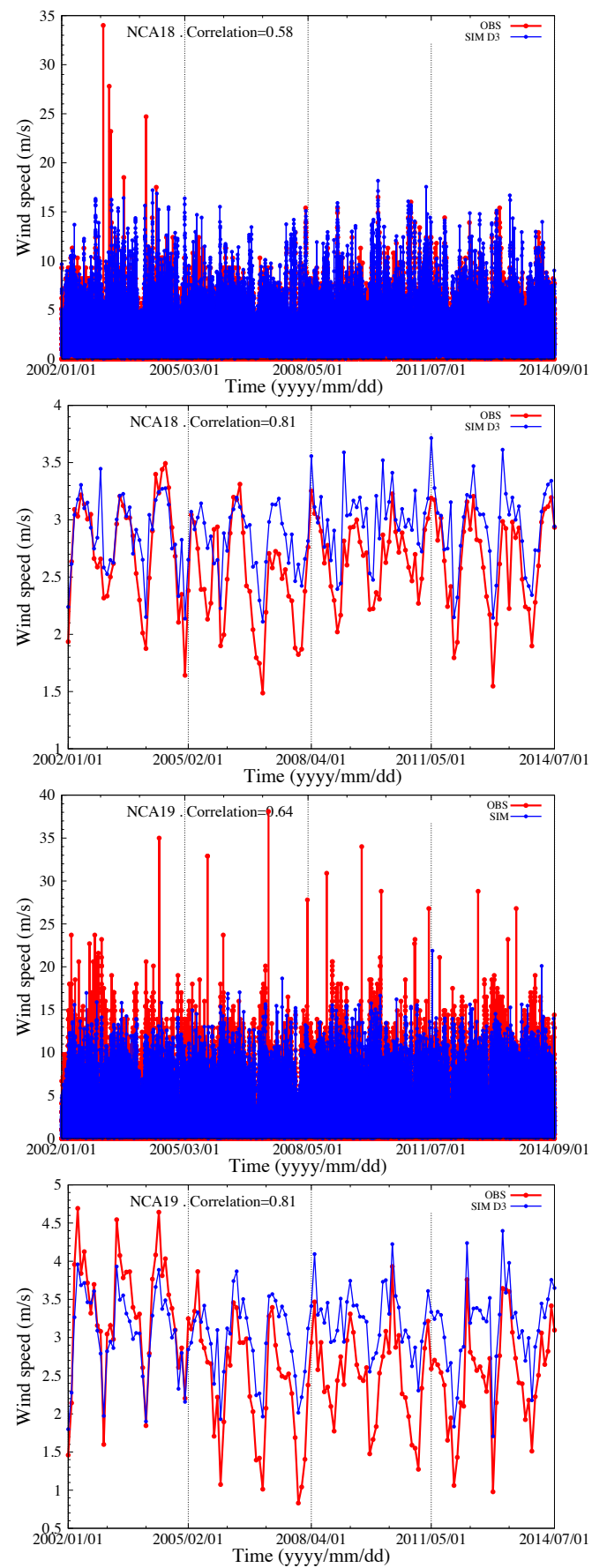
Figure S4 shows daily and monthly wind speeds at two sites (NCA18 and NCA19) located within D3, selected as an example because those sites have longer records within the dataset. The variability of the observed series is suitably described by the simulation. Correlations between the observed and simulated (nearest gridpoint) wind series at daily and monthly timescales are 0.58 (0.64) and 0.81 (0.81), respectively, at NCA18 (NCA19). The simulated wind adequately represents the variance of the observations at hourly timescales at NCA18 and seems to slightly underestimate it at NCA19. The observed monthly averages show slightly larger variability than simulated at both sites, which is an expected feature due to the temporal and spatial averaging effect of the model. The simulation seems to underestimate the variability of the observations before 2005 and to slightly overestimate it after 2005 at the two sites. Note that extreme data are present at both sites. The inter-annual variability of the larger wind speeds seems to overall agree in model and observations. However, the largest events registered in the observations stands out. As commented above, this is a common aspect in model simulations due to the smoothing effect related to the horizontal resolution limitations. Figure S5 compares the wind roses at the same sites. The observed and simulated distributions at NCA18 and NCA19 are slightly rotated but consistent, in general, with the orientation of the local topography. Similar conclusions can be reached for the remaining sites within the data set (not shown).

The identification of seasonal variations of the wind flow throughout the year is an important feature in validating the simulated wind field and in characterizing the regional and local wind variability. The annual distribution of daily maximum wind speed values on a 10-min basis is calculated at all sites within the database. In Figure S6a the corresponding box-whiskers diagram calculated over the period January 2002 to August 2014 at NCA19 is represented as an example. Both the reanalysis and the simulation represent adequately the annual wave of the largest winds with a minimum during the summer months and a maximum in winter. The range of variability is though better represented by the WRF simulation. It is noteworthy that the highest wind velocity values are by far better represented by the simulation compared to the reanalysis. The latter holds for all sites within the data set (not shown). Observing the inter-quartile distances, the range of variability tends to be wider in the case of the observations.
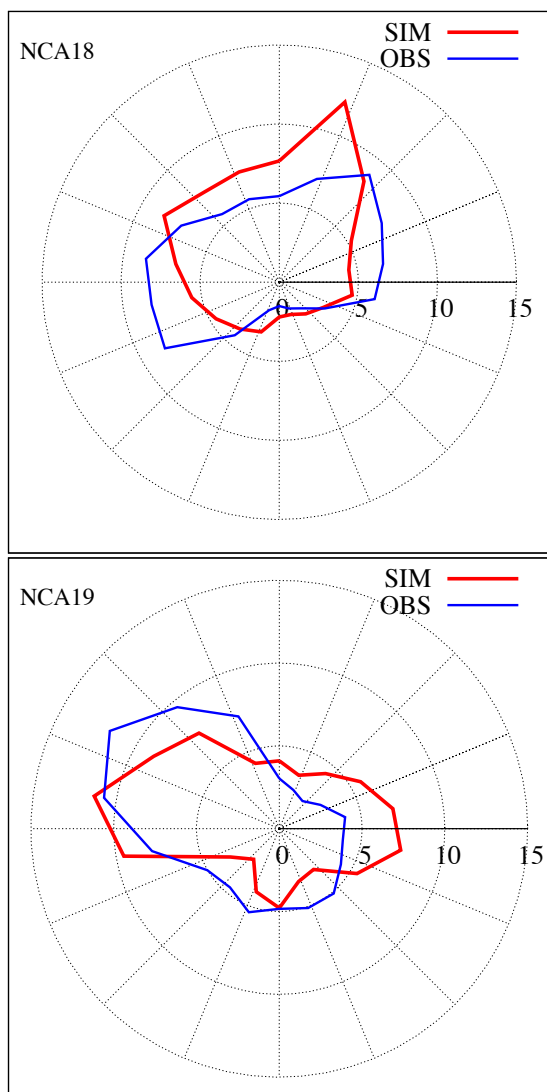
The long-term variability of the wind field from the simulation and observations is compared by analyzing the deviations from the long-term annual cycle evolution. This allows for evaluating the degree of agreement between the observations and the simulation at inter-annual timescales, notwithstanding the potential biases regarding the seasonal means commented above. The regional series of monthly mean and monthly maximum wind speed are represented herein.

Figure S6b (middle) shows the temporal evolution of the maximum regional wind for both observed (red) and simulated wind (gray and blue for the reanalysis and the regional model, respectively). The regional maximum is found by selecting, among all sites within the observations dataset, the maximum wind speed at each month. For the simulation, the same procedure is applied but selecting only the grid points co-located nearest to the corresponding observational sites to grant a better comparison. The correlation between observations and simulation (as well as for the reanalysis) is 0.46 ($p < 0.05$).
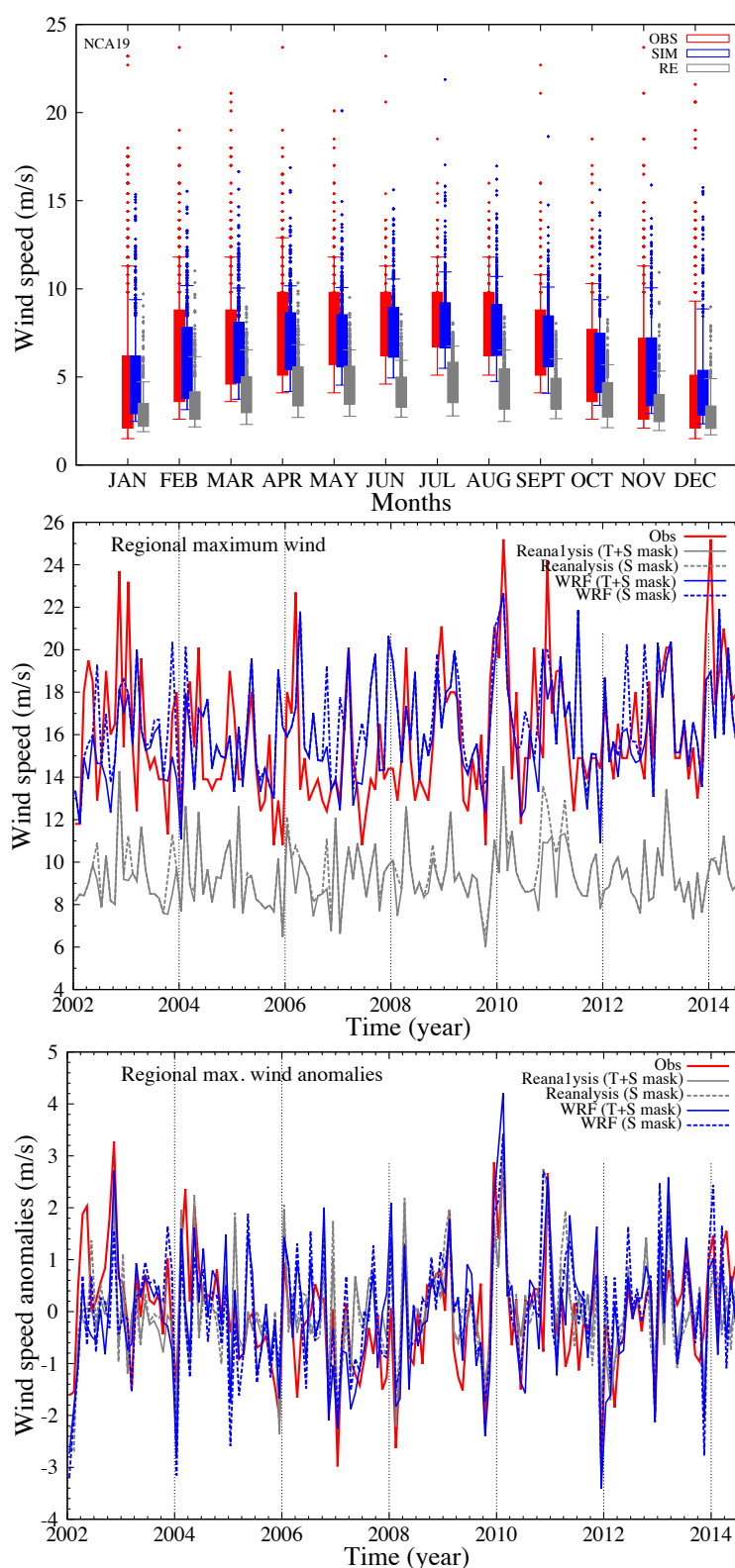
This correlation, although significant, is not high possibly owed to the fact that the regional maximum within a month might plausibly take place at different locations in the model compared to observations. Dashed lines indicate that the regional series are obtained by using only the grid points nearest to the observational sites (*spatial mask*). Solid lines indicate that the regional simulations as well as the reanalysis have been *temporally masked* in order to use exactly the same dates in the model as in the observations, thus, excluding values when observations are missing. In doing so, we learn about the impact of missing dates in the observations. Indeed, we observe a non negligible impact of masking the

Figure S4. Hourly (left) and monthly (right) wind speed time series from the WRF simulation (blue) and from observations (red) at NCAR18 (top) and NCAR19 (bottom).

Figure S**5.** Wind roses of hourly wind direction from the WRF simulation (blue) and from observations (red) at NCAR18 and NCAR19.

Figure S6. Top: box-whiskers plots showing the distribution of the daily maximum calculated from the observed 10-min wind values for each month during the period 2002–2014 at NCA19 for observations (red), the reanalysis (grey) and WRF simulation (blue). The lower (upper) box ranges represent the 25th (75th) percentile while the lower (upper) whiskers indicate the 10th (90th) percentile. Dots represent the values above the 75th percentile of the distribution considering all months. Middle: time series of regional monthly maximum wind speed. The regional series from the simulation was constructed by considering only grid points co-located to the observational sites. Solid lines indicate model averages using the data from the complete period (only spatial mask, no temporal masking). Dashed lines indicate the averages after masking the simulation with missing data as in the observations (spatio-temporal mask). Bottom: as in the middle panel but series are anomalies with respect to the annual cycle.

simulated series temporally, especially in the case of the regional model. WRF simulation shares similar levels of mean and variance with the observations, while the reanalysis clearly underestimates them.

The added value of the simulation to analyze high wind speeds relative to the reanalysis is distinguishable. It is also remarkable that the timing of the maximum wind events tends to harmonize well in magnitude between observations and simulation, albeit usually higher for the observations. Complementary, Figure S6c represents similar curves to those in Figure S6b but showing anomalies of wind speed relative to the monthly averages of regional maximum wind speed. The realism of the model simulations in depicting deviations from the mean wind is evident and, to some extent, improved in WRF relative to the reanalysis. This is particularly the case in the representation of the regional averages where the correlation calculated improves from 0.54 (reanalysis) to 0.68 (WRF).

The bias and variance ratios between simulated and observed daily mean (left) and daily maximum (right) wind speed (not shown) tend to be positive and smaller than 2 ms^{-1}, indicating that the simulation tends to overestimate the observational mean at some sites. At some locations, the daily maximum bias between simulation and observations is zero or close to zero, suggestive of a satisfactory ability of the regional model to represent the daily wind maxima. At a few sites, an underestimation of the wind maxima was also detected, being nonetheless the magnitude of the bias smaller than 1 ms^{-1}. The model presents a tendency to slightly overestimate the variance of the observed mean wind (not shown). When we evaluate the same for the daily maximum wind, the model presents a tendency to underestimate (overestimate) the variance over the western (eastern) part of the region.

The correlation between the simulated and observed daily maximum wind speed at each site ranges between 0.4 and 0.8. The regional averages present higher correlation values than the individual sites, and the regional simulation proves its added value with respect to the reanalysis in both cases (higher correlations with WRF simulation than with the reanalysis wind). Standard deviation ratios are comprised in the interval [0.75-1.25], demonstrating the tendency of the regional model to over-/under-estimate the observed maximum wind speed depending on the site as commented above. Finally, the RMSE values are compressed between 0.8 and 1.1 m/s.

Therefore, the daily bias, variance and correlation values are within the typical ranges for this type of problem. Local correlations range between 0.4 and 0.7 at hourly resolution improving slightly for the daily and monthly resolutions as commented above. The added value of the regional model relative to the reanalysis was evident at all resolutions and increased for daily and monthly timescales, since the local and regional maximum wind speed were also better represented by the WRF simulation.

Additionally, it was demonstrated that the regional model improved the representation of the annual wave of the wind speed relative to reanalysis. Increasing the horizontal resolution by means of a regional model simulation clearly improves the description of the temporal and spatial variability of the wind field and the highest wind episodes given by the reanalysis. Therefore, it seems pertinent to take advantage of the higher spatial coverage given by the regional simulation of the wind field to explore the spatial variability of the wind return levels over the region of interest (Section 4.3 of the main text).

2. Methodology

2.1. Statistical modeling of extreme winds

The paragraphs below include further detail about the extreme values statistical modeling, additional to the contents of Section 3.1 in the main text.

2.1.1. Probability distributions of extreme values

The central idea for the estimation of return values is that observed data has to be fitted to an appropriate theoretical distribution. Afterward, the return levels can be inferred from the properties of the distribution selected to describe the empirical population. By

default, extreme values are rare and unusual; therefore, the paucity of extreme data is an inherent feature and it represents the typical condition under which the EVT operates. The EVT [16] is based on the asymptotic argument. It postulates that there are mathematical models (probability distributions) that could provide a convergence limit of any variable, if the size of the population sample would grow infinitely.

The classic statistical theory of extremes assumes, under a wide range of hypothesis (among which the most decisive are the hypothesis of stationarity and the hypothesis of independence) that a series of values representing a block-maxima (e.g., the single highest value of any variable over a certain period) is distributed following a Generalized Extreme Value (GEV) distribution [17].

There is a pool of theoretical distributions that are cataloged under the umbrella of the GEV-type. Each of these theoretical distributions differs from each other in the behavior of the tail of the distribution. The latter is tantamount to say that specifically the largest values of the sample determine the shape of the distribution and that the focus is placed on how the tail converges to zero probability.

The three types of Block-Maxima distributions termed as *extreme value distributions* are:

I   Gumbel

$$G(z) = exp\left\{-exp[-(\frac{z-b}{a})]\right\}, -\infty < z < \infty \tag{1}$$

II   Fréchet

$$G(z) = \begin{cases} 0, & z \leq b \\ exp\left\{-(\frac{z-b}{a})^{-\alpha}\right\}, & z > b \end{cases} \tag{2}$$

III   Weibull

$$G(z) = \begin{cases} exp\left\{-[-(\frac{z-b}{a})^{\alpha}]\right\}, & z < b \\ 1, & z \geq b \end{cases} \tag{3}$$

where $G(z)$ is the probability distribution of the z extreme values population, $a > 0$ is the scale parameter, b is the location parameter and α is the shape parameter only in the case of Fréchet and Weibull families [16].

The generalization of the three types of families in a single model is denoted as the Generalized Extreme Value Distribution (GEVD):

$$G(z) = exp\left\{-[1 + \xi(\frac{z-\mu}{\sigma})]^{-1/\xi}\right\} \tag{4}$$

In the general formulation of the POT families, the Generalized Pareto Distribution follows:

$$H(y) = 1 - (1 + \frac{\xi y}{\bar{\sigma}})_+^{-1/\xi}, y > 0 \tag{5}$$

where $H(y)$ is the probability distribution of the y extreme values population with σ, ξ and μ as in $G(z)$ above (Eq. 4).
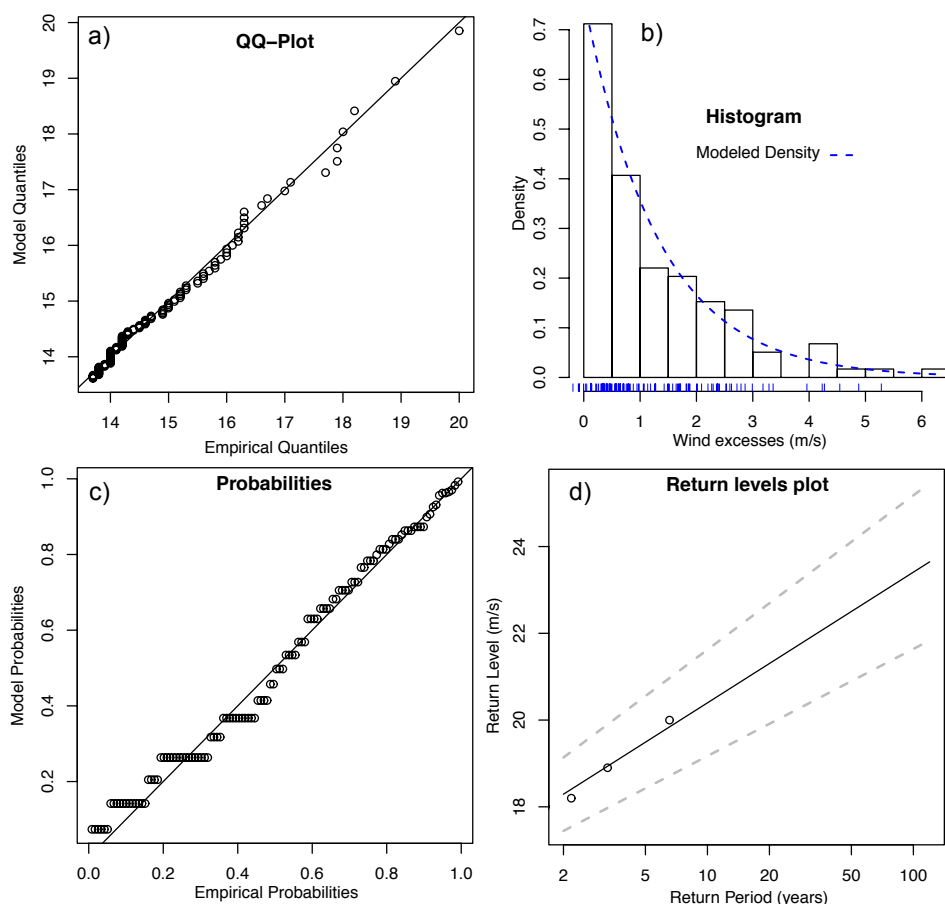
2.1.2. Return levels of extremes

The definition of the return levels follows the equation:

$$z_p = \begin{cases} \mu - \frac{\sigma}{\xi}[1 - \{-log(1-p)\}^{-\xi}], & if \quad \xi \neq 0 \\ \mu - \sigma log\{-log(1-p)\}, & if \quad \xi = 0 \end{cases} \tag{6}$$

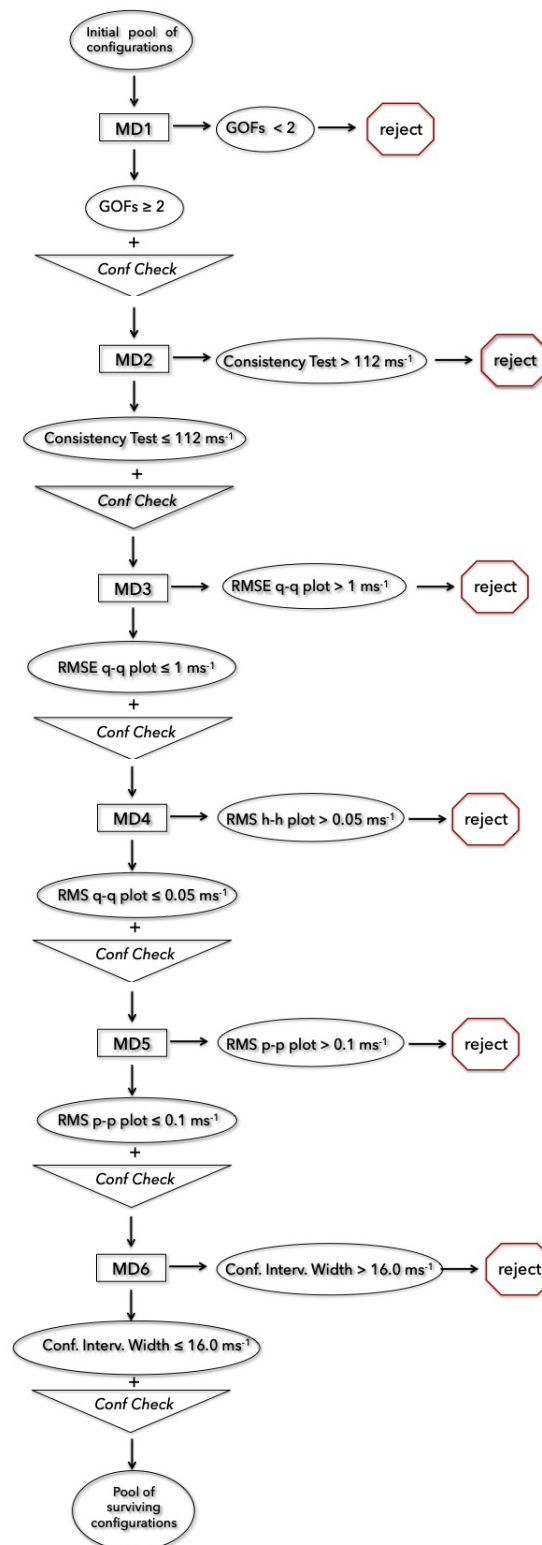## 2.2. Constraining the methodological uncertainty

Figure S7 shows the plots that are used to design the sequence of filters applied in this section: q-q, h-h, p-p and RL plots are represented in Figures S7a, S7b, S7c and S7d, respectively.

Figure S**7.** Empirical vs. theoretical distributions used as model diagnostics: a) qq-plot (MD3) indicating the empirical against the theoretical quantiles, b) hh-plot (MD4) representing the empirical against the theoretical histograms, c) pp-plot (MD5) that illustrates the empirical and theoretical probabilities based on the corresponding probabilities distributions and c) Return Levels plot (MD6) with the empirical points as explained in the main text (Section 3.2, Figure 2).

Figure S8 illustrates the sequence of filters and tests applied in Section 3.2 of the main text and the requirement that each model diagnostic (MDi) imposes to the pool of experiments that survive the preceding filter. *GOF* stands for Goodness-of-Fit test, RMSE *x-x* plot represents the corresponding Root Mean Square Error (being *x-x*= q-q, h-h and p-p plot, respectively) and *Conf. Interv. Width* refers to the width of the corresponding experiment upper confidence interval.

Figure S**8.** Sequence of filters designed to detect non-reliable experiment in the Methods Section (Section 3.2 in the main text).

References

1. Jiménez, P.A.; GonzÍez-Rouco, J.F.; J.Navarro.; Montávez, J.P.; Garcia-Bustamante, E. Quality assurance of surface wind observations from automated weather stations. *J. Atmos. Oceanic Technol.* **2010b**, *27*, 1101–1122.
2. Lucio-Eceiza, E.E.; González-Rouco, J.F.; Navarro, J.; Beltrami, H. Quality Control of surface wind observations in North Eastern North America. Part I: Data Management Problems. *Journal of Atmospheric and Oceanic Technology* **2018**, *35 (1)*, 163–182. doi:10.1175/JTECH-D-16-0204.1.
3. Lucio-Eceiza, E.E.; González-Rouco, J.F.; Navarro, J.; Beltrami, H.; Conte, J. Quality Control of surface wind observations in North Eastern North America. Part II: Measurement Errors. *Journal of Atmospheric and Oceanic Technology* **2018**, *35 (1)*, 183–205. doi:10.1175/JTECH-D-16-0205.1.
4. Dee, D.P.; Uppala, S.M.; Simmons, A.J.; Berrisford, P.; Poli, P.; Kobayashi, S.; Andrae, U.; Balmaseda, M.A.; Balsamo, G.; Bauer, P.; others. The ERA-Interim reanalysis: configuration and performance of the data assimilation system. *Quart. J. Roy. Meteor. Soc.* **2011**, *137*, 553–597.
5. Trenberth, K., Ed. *Atmospheric Reanalyses: A Major Resource for Ocean Product Development and Modeling*. Proceedings of OceanObs09: Sustained Ocean Observations and Information for Society, 2010.
6. Jiménez, P.A.; González-Rouco, J.F.; García-Bustamante, E.; Navarro, J.; Montávez, J.P.; de Arellano, J.V.G.; Dudhia, J.; Roldán, A. Surface wind regionalization over complex terrain: evaluation and analysis of a high resolution WRF numerical simulation. *J. Appl. Meteor. Climatol.* **2010**, *49*, 268–287.
7. Jiménez, P.A.; Dudhia, J.; González-Rouco, J.F.; Navarro, J.; Montávez, J.P.; Garcia-Bustamante, E. A Revised Scheme for the WRF Surface Layer Formulation. *Mon. Wea. Rev.* **2012**, *140*, 898–918.
8. Mlawer, E.J.; Taubman, S.J.; Brown, P.D.; Iacono, M.J.; Clough, S.A. Radiative transfer for inhomogeneous atmosphere: RRTM, a validated correlated-k model for the longwave. *J. Geophys. Res.* **1997**, *102 (D14)*, 16663–16682.
9. Dudhia, J. Numerical study of convection observed during the winter monsoon experiment using a mesoscale two-dimensional model. *Journal of the Atmospheric Sciences* **1989**, *46*, 3077–3107.
10. Kain, J.S.; Fritsch, J.M. A one-dimensional entraining/detraining plume model and its application in convective parameterization. *Journal of the Atmospheric Sciences* **1990**, *47*, 2784–2802.
11. Kain, J.S.; Fritsch, J.M. Convective parameterization for mesoscale models: The Kain-Fritcsh scheme, The representation of cumulus convection in numerical models. *Amer. Meteor. Soc* **1993**, p. 246.
12. Hong, S.Y.; Noh, Y.; Dudhia, J. A new vertical diffusion package with an explicit treatment of entrainment processes. *Mon. Wea. Rev.* **2006**, *134*, 2318–2341.
13. Lin, Y.L.; Farley, R.D.; Orville, H.D. Bulk parameterization of the snow field in cloud model. *J. Appl. Meteor. Climatol.* **1983**, *22*, 1065–1092.
14. Chen, F.; Dudhia, J. Coupling an advanced land-surface/hydrology model with the Penn State/NCAR MM5 modeling system. Part.I: Model implementation and sensitivity. *Mon. Wea. Rev.* **2001**, *129*, 569–585.
15. Skamarock, W.C.; Klemp, J.B.; J.Dudhia.; Gill, D.; Barker, D.M.; Wang, W.; Powers, J.G. A description of the advanced research WRF Version 2. *Technical Report TN-468+STR, NCAR* **2005**.
16. Coles, S.; Bawa, J.; Trenner, L.; Dorazio, P. *An introduction to statistical modeling of extreme values*; Vol. 208, Springer, 2001.
17. Larsén, X.G.; Mann, J.; Rathmann, O.; Jørgensen, H.E. Uncertainties of the 50-year wind from short time series using Generalized Extreme Value Distribution and Generalized Pareto Distribution. *Wind Energy* **2015**, *18*, 59–74.